

Prediction of the mechanical response of canine humerus to three-point bending using subject-specific finite element modelling

Proc IMechE Part H:
J Engineering in Medicine
2016, Vol. 230(7) 639–649
© IMechE 2016
Reprints and permissions:
sagepub.co.uk/journalsPermissions.nav
DOI: 10.1177/0954411916644269
pjh.sagepub.com


Cédric P Laurent^{1,2}, Béatrice Böhme³, Marlène Mengoni^{1,4},
Vinciane d'Otreppe¹, Marc Balligand³ and Jean-Philippe Ponthot¹

Abstract

Subject-specific finite element models could improve decision making in canine long-bone fracture repair. However, it preliminary requires that finite element models predicting the mechanical response of canine long bone are proposed and validated. We present here a combined experimental–numerical approach to test the ability of subject-specific finite element models to predict the bending response of seven pairs of canine humeri directly from medical images. Our results show that bending stiffness and yield load are predicted with a mean absolute error of 10.1% ($\pm 5.2\%$) for the 14 samples. This study constitutes a basis for the forthcoming optimization of canine long-bone fracture repair.

Keywords

Finite element modelling, subject-specific, canine bone material properties, bending test, canine humerus

Date received: 13 July 2015; accepted: 21 March 2016

Introduction

Long-bone fracture constitutes a common reason for medical consultation within veterinary orthopaedic services,^{1,2} as emphasized by the substantial recent literature concerning the choice of adapted implants.^{3–6} Associated surgical interventions are often complex given that each fracture has its own particularities. Canine bone fracture repair differs from the human case in the sense that (1) the physiological characteristics and morphology of the injured bones in animals vary considerably;⁷ (2) the animal is not able to limit its activity during the post-operative period, which may lead to premature overloading; and (3) the surgeon is often confronted to cost limitations concerning orthopaedic material. As a result, the treatment of such fractures (implant type, dimension, location, etc.) depends to some extent on the surgeon's experience, who tries to find a trade-off between a minimum stiffness required for fracture stabilization and a sufficient flexibility essential for bone remodelling. Although available handbooks guide the surgeon in the choice of a suited treatment for each particular fracture, they are still based on empirical knowledge, and there is a lack of studies assessing the effect of different treatment types

on the biomechanical properties of the reconstructed bone. This insufficient knowledge may partly explain the complications that are still frequent in the field of canine fracture repair.^{8,9}

In order to improve the surgical procedure, *ex vivo* experiments^{10,11} as well as numerical biomechanical studies^{12–14} have been reported. Indeed, numerical approaches, such as finite element (FE) modelling, may enable to evaluate non-invasively the effect of various implants or their combination on the same bone sample. However, these FE studies are often based on simplistic bone models (i.e. elastic, linear, homogeneous

¹Department of Aerospace and Mechanical Engineering, University of Liège, Liège, Belgium

²CNRS, LEMTA, UMR 7563, Université de Lorraine, Vandoeuvre-lès-Nancy, France

³Department of Clinical Sciences, Faculty of Veterinary Medicine, University of Liège, Liège, Belgium

⁴Institute of Medical and Biological Engineering, School of Mechanical Engineering, University of Leeds, Leeds, UK

Corresponding author:

Cédric P Laurent, CNRS, LEMTA, UMR 7563, Université de Lorraine, 2 avenue de la forêt de Haye, F-54502 Vandoeuvre-lès-Nancy, France.
Email: Cedric.laurent@univ-lorraine.fr

cortical and trabecular tissues, etc.). A milestone in delivering relevant data in a subject-specific approach consists of including the bone external geometry and heterogeneous material properties from the information available in computed tomography (CT) images. Such subject-specific FE approaches have been developed in human long-bone analysis and satisfyingly predicted the failure risk in proximal femur.^{15–18} However, available studies in human have often led to moderately accurate results as far as the prediction of the global biomechanical response of long bones are concerned, probably due to accumulating inherent approximations throughout the model generation. Particularly, it is not clear whether the consideration of density-dependent material properties leads to better results than the modelling of long bone with two materials (trabecular and cortical tissues) separated from a density criterion. The interest of considering anisotropic material properties is also not clear. Moreover, if one wants to extend these subject-specific FE models to canine bone, a supplementary difficulty will come from the variability of bone material properties from one breed to another,¹⁹ and from the absence of data concerning relationships between CT information and bone material properties for dogs.

Such FE models are usually validated using *ex vivo* mechanical tests such as bending,^{20,21} torsion,²² or compression.^{17,23} These combined experimental–numerical approaches require that a particular attention is paid to the application of similar boundary conditions (BC), such as load application and displacement restriction, in the experimental and computational setups.²⁴

In the present contribution, the hypothesis was that subject-specific FE models are able to predict the global mechanical response of canine long bones to three-point bending tests. The aims of this work were therefore (1) to provide a direct subject-specific validation of canine long-bone FE models including a novel

density–elasticity law and (2) to assess the requirements for the bone material model to replicate measured *ex vivo* behaviour.

Material and methods

A combined experimental and computational approach was developed to validate the FE models with *ex vivo* three-point bending data, that is, overall load/deflection behaviour and local fracture patterns. All dynamic FE analyses were performed using the in-house non-linear implicit FE code Metafor (metafor.ltas.ulg.ac.be).

Specimen preparation, imaging, and mechanical testing

Eight pairs of canine humeri were initially harvested from adult dogs euthanized for reasons unrelated to this study. After harvesting, one dog (i.e. one pair of humeri) was excluded from this study due to the observation of severe knee arthrosis. Dog weights finally ranged from 19 to 39 kg. Soft tissues were carefully removed and samples were wrapped in saline-soaked sponges and stored at -0°C . Samples were prepared for three-point bending mechanical tests at room temperature. In order to accurately control the location of the bones within the custom bending stand and to restrict rotations around the bone diaphysis axis during the bending tests, the epiphyses were embedded into $60 \times 60 \times 60 \text{ mm}^3$ moulds made of two-component polymeric resin (Motip[®], MOTIP DUPLI B.V, Wolvega, Nederland) (Figure 1). A particular attention was paid to define resin moulds' orientation with respect to the bone sample position in a reproducible way. First, we used the origin of the medial and lateral collateral ligaments as anatomical landmarks to define a reference axis. Then, the distal resin mould was created in such a way that this anatomical reference axis

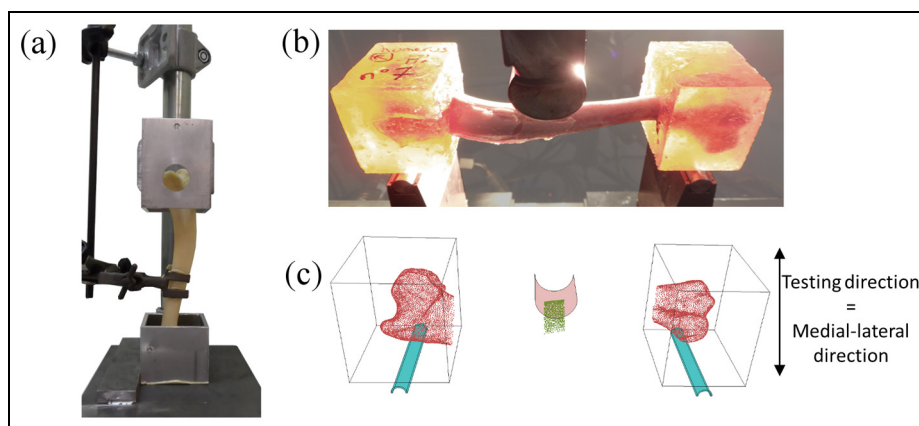


Figure 1. Experimental and simulated bending test on canine humerus: (a) preparation of bone samples using a custom jig to align resin moulds, (b) bone samples embedded in resin moulds were mounted in a custom bending stand, and (c) the bending tests were simulated by simplifying the resin moulds with single hexahedrons linked to the bone surface (red dots) via artificial springs. A sticking contact condition was considered between the bending tool and the bone surface (green dots), while contact–friction interaction was considered between the resin moulds and the bending stand (blue cylinders).

was parallel to two surfaces of the resin block (namely, its cranio-caudal and proximal–distal surfaces). The second mould was perfectly aligned with the first one, using custom-made jig (Figure 1(a)).

The samples were imaged using a CT scanner (Siemens SOMATOM at 120 kVp) with a slice thickness of 0.75 mm and a spatial resolution of 0.1445 mm. A phantom (Siemens BMD calibration phantom²⁵) was used to calibrate the bone densities with respect to the Hounsfield Units (HU) issued from the CT acquisition.^{18,26} Particular attention was paid to keep the samples packed in saline-soaked wraps throughout the procedure in order to avoid tissue dehydration. The following relation was obtained

$$\rho = 4.9332 \times 10^{-4} \text{HU} + 0.9839 \quad (1)$$

Samples were placed on a custom adjustable bending stand (Figure 1(b)) made of two steel half-cylinders. The cylinders' positions were adjusted so that they were in contact with the middle of each resin mould in the axial direction of the bone. The bending tool consisted in a cylindrical punch located longitudinally at half the distance between the two resin moulds. The stand was mounted in a 100-kN servo-hydraulic testing machine (load cell: XForce HP 5 kN; Zwick/Roell, Ulm, Germany). A medial–lateral displacement was applied to the bending tool at a speed of 0.2 mm s⁻¹ after a preload of 50 N. The samples were tested until complete fracture. Tool displacement (hereafter called deflection) and vertical force (i.e. shear force) were recorded. Two high-speed cameras (Vision Research v7.3) recording 1000 frames per second were used in order to visualize the fracture onset.

Finite element modelling

Each tested sample was modelled with a subject-specific approach. The geometry of the bone was built from the three-dimensional (3D) CT data using 3D Slicer²⁷ (<http://www.slicer.org>) for segmentation and a dedicated in-house algorithm²⁸ for the generation of smooth multi-region surface meshes. The bone volume mesh was obtained using TetGen (WIAS, Berlin, Germany), generating linear tetrahedra. Final mesh size was issued from a mesh dependency analysis reported hereafter.

The resin moulds were not meshed in the FE model but considered as single deformable hexahedrons whose coordinates were automatically computed from the boundaries of resin moulds in the surface mesh (Figure 1(b)). Resin was considered linear elastic, with an elastic modulus of 900 MPa characterized from preliminary experiments. Elements were assigned a density issued from the calibration phantom and equal to 1 g cm⁻³ for resin. The interaction between the bone and the resin moulds was modelled using springs (arbitrary stiffness of 100 N mm⁻¹) linking the hexahedron nodes with each of the bone surface nodes located within the resin moulds (Figure 1(b)) in order to constrain the

relative displacement between bone and resin. This numerical representation of the resin blocks is totally equivalent to a penalty formulation in contact algorithms with bilateral restrictions to enforce the continuity of the displacement field at the interface between bone and resin. The proximal resin mould was restrained in the cranio-caudal direction.

The bending stand was modelled as two rigid half-cylinders located longitudinally at the middle of each resin moulds. The frictional contact condition between the resin moulds and the bending stand was modelled with a Coulomb's law, with static and dynamic friction coefficients set at 0.7, corresponding to a dry static contact between steel and steel.²⁹ This value was chosen due to the lack of published value for resin–steel contact. Each half-cylinders of the bending stand were restrained in their 6 degrees of freedom.

The bending tool was modelled as a rigid half-cylinder located, as marked experimentally, at half the distance between the two resin moulds. Displacement was applied to the tool in the medial–lateral direction. Contact between the bending tool and the bone surface was modelled as sticking contact.

A sensitivity analysis was performed analysing the effect of the resin properties, the stiffness of the springs used to attach bone to resin blocks, and the friction coefficient between resin and stand on the predicted bone stiffness and yield load. Load–deflection curves were obtained as the sum of the medial–lateral component of the contact force and the tool displacement at each time step. The experimental preload was mimicked by excluding the initial forces below 50 N from the simulation results.

For each sample, user interaction was only needed for the image segmentation step. To avoid user variation, all other steps of the model creation and analysis were automated, based on the size of the samples extracted from the segmented data. All FE analyses were performed using local high-performance computing (HPC) facilities (parallel computation on 144 cores).

Bone material models

Three different materials models were considered for the bone: a density-dependent transversely isotropic model, a density-dependent isotropic model, and a two-material isotropic model (one material model for cortical bone and one for trabecular bone).

For the density-dependent models, material parameters were mapped against the HU values from the CT scans starting from equation (1). The following mapping procedure was applied: (1) for each mesh element, the smallest rectangular box that embraced the tetrahedron was defined; (2) for each voxel included within this box, material properties (see the following section) were computed from the density computed from the HU field; and (3) material properties were averaged on this box and assigned to the mesh element.

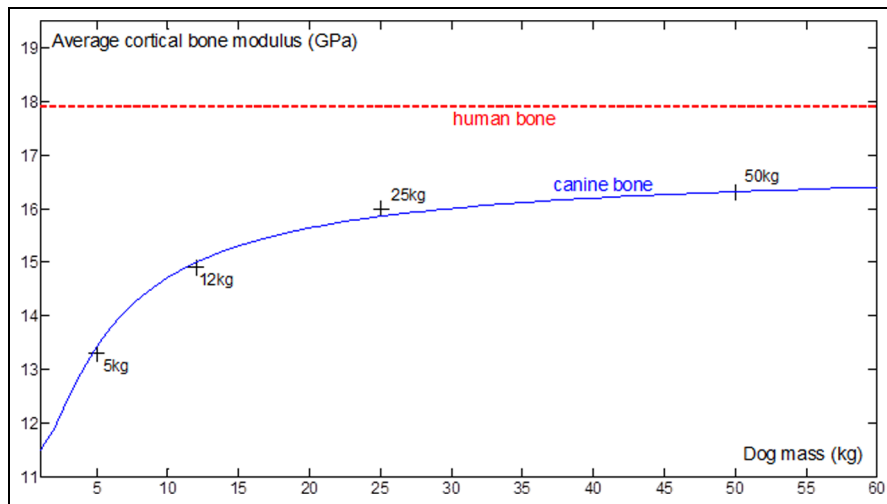


Figure 2. Determined relation between canine bone properties as a function of mass based on existing data¹⁹ and human bone properties.

A particular attention was paid to reduce the partial volume artefacts: to this end, we first separated the mesh elements that had at least one point belonging to the bone surface (*outer cells*) from the other mesh elements (*inner cells*). Each outer cell was then associated to its closest inner cell and was assigned the HU value of its associated inner cell when it was higher than its own HU value. This procedure significantly reduced the partial volume artefact, provided that the bone cortical wall was described by a sufficient number of mesh elements, that is, that the mesh was sufficiently dense.

It is known that the properties of canine bone depend on dog mass.¹⁹ Therefore, a density–elasticity relationship had to be derived for canine bone. It would indeed not be justified to use a unique density–elasticity relationship determined from human bone. Published experimental data¹⁹ reported the elastic moduli of canine cortical bone as a function of dog breed: 13.3 GPa (dog mass = 5 kg), 14.9 GPa (dog mass = 12 kg), 16 GPa (dog mass = 25 kg), and 16.3 GPa (dog mass = 50 kg). Comparing that data to an average reported elastic modulus of 17.9 GPa for human cortical bone,³⁰ the following relation between human data and canine data was extrapolated (using a common mean-square method)

$$E_{\text{canine}}(\rho) = E_{\text{human}}(\rho) \times (0.3 \exp(-5/m) + 0.64) \quad (2)$$

where m is the dog mass. This relation is illustrated in Figure 2 and assumes that bone properties depend only on dog mass and not on the breed.

This canine-to-human relation was used to weight existing density–elasticity relationships validated for human data. For the density-dependent transversely isotropic model, bone was considered as an elastoplastic material without distinction between cortical and trabecular tissues (except for density). The elastic part of the model was built from relation (2) and using an

orthotropic elasticity–density relationship for human bone in tension³¹

$$\begin{aligned} E_l &= 2065\rho^{3.09} & G_{ll} &= 0.29E_l \\ E_t &= 2314\rho^{1.57} & G_{tt} &= 0.2E_l \end{aligned} \quad (3)$$

where E_l and E_t are the elastic moduli (MPa) in the longitudinal and transverse directions, respectively; G_{ll} and G_{tt} are the shear moduli (MPa); and ρ (g cm^{-3}) is the apparent density issued from CT calibration. These relations valid for human bone were weighted using relation (2) in order to model canine bone. Asymmetric elastic material properties were assumed by considering that the elastic modulus was 6% higher in compression than in tension.³²

The global longitudinal direction was automatically computed for each sample, based only on the central third of the bone (representing the diaphysis, see Figure 3). The mesh nodes belonging to the bone surface and included in this part were selected and used to compute a least-square line defined as the longitudinal direction. The transverse direction was defined

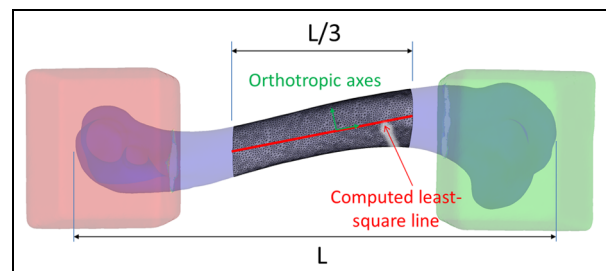


Figure 3. Calculation of orthotropic axes (longitudinal and transverse for a transversely isotropic model) from the central third of the bone. Longitudinal direction is defined as the computed least-square line of the mesh nodes included in the bone diaphysis surface.

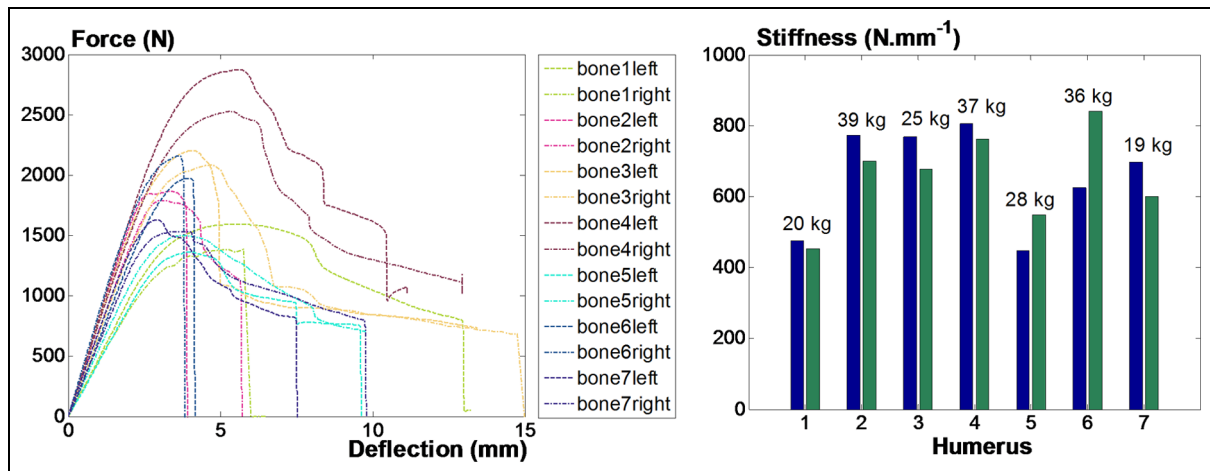


Figure 4. (Left) Bending responses of the 14 humeri and (right) bending stiffness of the seven pairs of humeri, emphasizing the large inter- and intra-variability of measured responses.

perpendicularly to this direction, in a plane containing the tool displacement vector.

The yield surface was defined through a von Mises criterion with linear isotropic hardening. The initial yield stress was obtained from the yield strain of 0.73% reported for human cortical bone³³ and the mean elastic modulus (defined as the average of longitudinal and transverse moduli) following the relation

$$\sigma_y = \frac{0.0073 (E_l + E_t)}{2} \quad (4)$$

The role of the longitudinal stress was therefore considered predominant in the bone yield. Post-yield hardening was set as 5% of the initial, density-dependent, mean elastic moduli.³⁴

The same procedure was applied for the density-dependent isotropic model. The unique Young's modulus was defined as the mean of the computed longitudinal and transverse modulus for a given bone density (relation (3)) weighted by the correction coefficients given in relation (2). Yield was modelled identically to the previous model.

For the two-material isotropic model, trabecular and cortical canine tissues were modelled with Young's modulus of 750 MPa and 15 GPa, respectively, and a Poisson's ratio of 0.3.³⁵ Cortical and trabecular tissues were separated using a threshold in terms of HU values. Cortical tissue was assumed for HU values superior to either 600 or 400 HU in order to assess the sensitivity to this parameter. Yield was modelled identically to the previous models.

Statistical analysis

For each tested bone, bending stiffness (least-square linear regression of the linear part of force–deflection curve passing through the origin) and yield load (intersection between a parallel to this linear regression with a 0.1 mm offset and the force–deflection curve) were extracted and compared between the experimental and computational data.

In order to emphasize the statistical significance of our model, we performed various statistical analyses from our experimental results (14 samples from 7 dogs) and our numerical results (56 models: 14 density-dependent transversely isotropic models, 14 density-dependent isotropic models, 14 two-material isotropic models with a segmentation threshold of 400HU, and 14 others with a segmentation threshold of 600HU). Analysis of variance (ANOVA) was used as the common test to quantify the difference between two sets of data, with a default *p* value of 0.01 (when not detailed).

Results

Experimental results

Experimental results for the seven pairs of humeri are represented in Figure 4. A large intra- and inter-variability was observed: as an example, a mean difference of 14.6% in stiffness between the left and right humerus of the same dog. Left and right humeri of the same dog were, however, not different (both in terms of stiffness and yield load) in the sense of an ANOVA analysis. The coefficient of variation (ratio between standard deviation and mean) of the stiffness is equal to 20.2%. The data showed a weak correlation between dog mass and mean humerus stiffness (correlation coefficient of 0.65). While the failure was immediate for six samples, it was more progressive for the others, and therefore, no clear fracture pattern was visible.

Computational results

The meshes resulting from the reconstruction of the segmented CT images together with the mapping procedure are represented in Figure 5 for all bone samples. Bone mesh made of approximately 300,000 tetrahedral linear elements (60,000 nodes) led to a relative difference of 2.5% on strain energy density (SED) and 1.4% on stiffness compared to the values obtained for

Table 1. Sensitivity analysis of the computational results: effect of resin properties, spring stiffness, and friction coefficient between bending stand and resin on predicted bone stiffness and yield load.

Resin modulus (MPa)	Predicted stiffness (N mm^{-1})	Predicted yield load (N)	Spring stiffness (N mm^{-1})	Predicted Stiffness (N mm^{-1})	Predicted yield load (N)	Friction coefficient	Predicted stiffness (N mm^{-1})	Predicted yield load (N)
100	548.3	1500.2	1	532.3	1497.9	0.5	507.3	1425.9
500	548.3	1500.2	10	544.2	1500.1	0.6	527.2	1462.2
900	548.3	1500.2	100	548.8	1500.2	0.7	548.8	1500.2
1300	548.3	1500.2	1000	558.0	1489.4	0.8	572.2	1539.7
1700	548.3	1500.2	10,000	544.0	1508.8	0.9	595.1	1590.8

The star indicates a significant difference between a set of parameters and the selected parameters in the presented simulations.

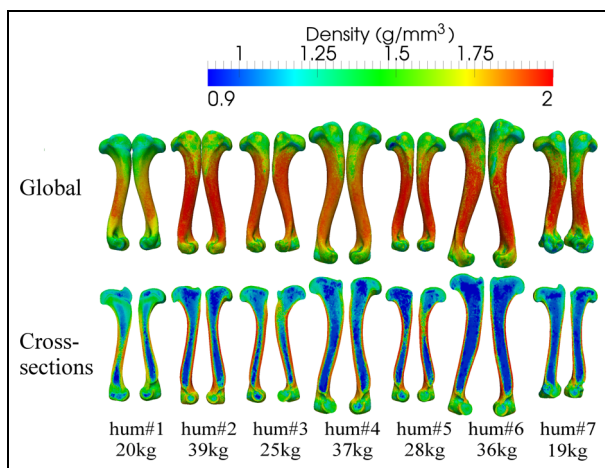


Figure 5. Bone meshes resulting from the reconstruction of segmented CT images together with the mapping procedure. The colour code corresponds to the computed densities (g mm^{-3}) assigned to each mesh element from HU values.

160,000 nodes. The results of the sensitivity study for one humerus are reported in Table 1. These data emphasize that the simulation results are not sensitive to resin properties, indicating that the resin does not deform substantially during the bending test. Moreover, the simulation results are very slightly sensitive to the stiffness of springs used to attach bone to resin (2% of deviation for a variation of five orders of magnitude). A stiffness of 100 N mm^{-1} (i.e. of the same order of magnitude than the bone bending stiffness) has been consequently selected for every simulations. However, this sensitivity study emphasizes that the friction coefficient does have an effect on predicted stiffness and yield load. A friction coefficient of 0.7 has been chosen for the simulations due to the lack of existing data, as long as such data are difficult to measure experimentally.

For the density-dependent transversely isotropic model of the 14 samples, the bending stiffness was predicted with a maximum error of 21.7% (absolute value of the mean error = $10.1\% \pm 5.2\%$). The yield load was predicted with an absolute value of the mean error $11\% \pm 11.3\%$, but was unsatisfyingly predicted for one sample over the 14 samples (maximum error = 43.5%,

see Figure 6). Correlation coefficients between predicted and measured values were 0.86 for stiffness and 0.74 for yield load. A Bland–Altman representation of the simulation results obtained with this model has also been provided (Figure 7): it clearly illustrates the good prediction ability of this model. However, this representation clearly emphasizes that the values of bending stiffness and yield load are badly predicted for one sample (6 right).

Results of the different models were confronted to experimental results in the sense of ANOVA statistical tests, and the p values issued from these tests are gathered in Table 2, under the null hypothesis that experimental and simulations results have the same mean (i.e. if the p value is near to zero, experimental and simulation results are significantly different). From this analysis, it is clear that the density-dependent transversely isotropic model is the most predictive model among the four different models tested, and especially compared to the density-dependent isotropic model, as illustrated in Figure 8. Surprisingly, the computational results are better in the case of the two-material isotropic models (no matter the segmentation threshold) than in the case of density-dependent isotropic models.

Results of the FE simulations for the two-material isotropic model are represented in Figure 9, with trabecular and cortical tissues being separated either from HU values of 400 or 600 HU in order to quantify the sensitivity of the bending response to this threshold. There is no statistical difference between the two threshold values used to separate cortical from trabecular tissue in the case of two-material models.

Discussion

Model accuracy

A FE mesh of 60,000 nodes showed to be a converged mesh for the bone stiffness and SED. A satisfying prediction of bone stiffness was obtained for every sample, whereas the yield load was satisfyingly predicted for 13 over 14 samples. The reported computational results were insensitive to the properties assigned to the resin block holding the bone epiphysis; this indicates that resin blocks do not deform much during the

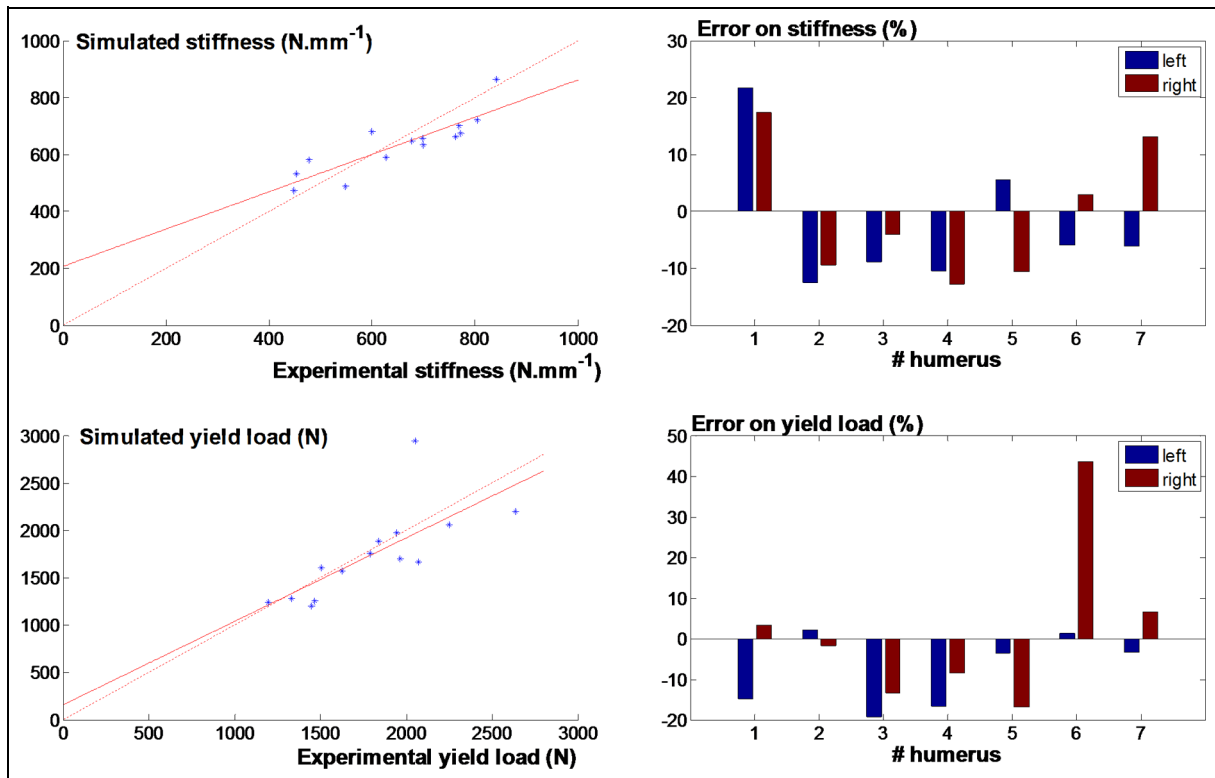


Figure 6. (Left) Experimental versus simulated stiffness and yield load for the 14 bone samples and for the density-dependent transversely isotropic model. The dashed line represents a perfect prediction (simulation = experiments), whereas the continuous line represents the linear fitting of the data. (Right) Prediction error on stiffness and yield load for the seven pairs of humeri.

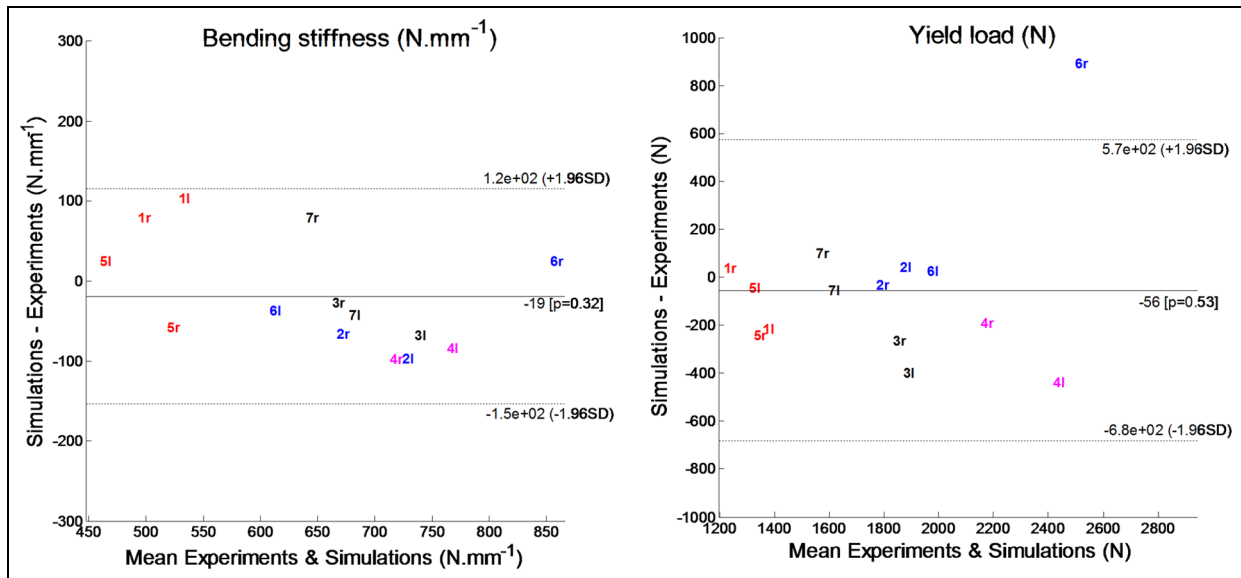


Figure 7. Bland–Altman representation of the results obtained for the density-dependent transversely isotropic model in terms of bending stiffness (left) and yield load (right). Points are represented with the corresponding sample name (r = right, l = left).

simulations. The computational representation of those blocks is thus a good approximation of the block behaviour and interaction with the bone.

Using the verified and validated non-linear FE software Metafor^{36–39} to analyse long-bone three-point bending tests permits high automation of the model

pre- and post-processing steps. This reduces user variability to the image segmentation step only. All other parameters, especially as far as the definition of model BCs representative of the experimental conditions is concerned, are subject only to the experimental variability.

Table 2. Confrontation of the computational and experimental results in terms of predicted yield load and bending stiffness.

	Stiffness (N mm^{-1})				Yield load (N)			
	Trans. Iso.	Iso.	400 HU	600 HU	Trans. Iso.	Iso.	400 HU	600 HU
p value of the ANOVA test	0.67	2.48×10^{-4}	0.43	0.17	0.74	4.13×10^{-5}	0.18	0.08

The p value of ANOVA tests are given for density-dependent transversely isotropic models (trans. iso.), density-dependent isotropic models (iso.), and two-material isotropic models with segmentation threshold of 400 and 600 HU. Low p values indicate a significant difference between experimental and simulation results.

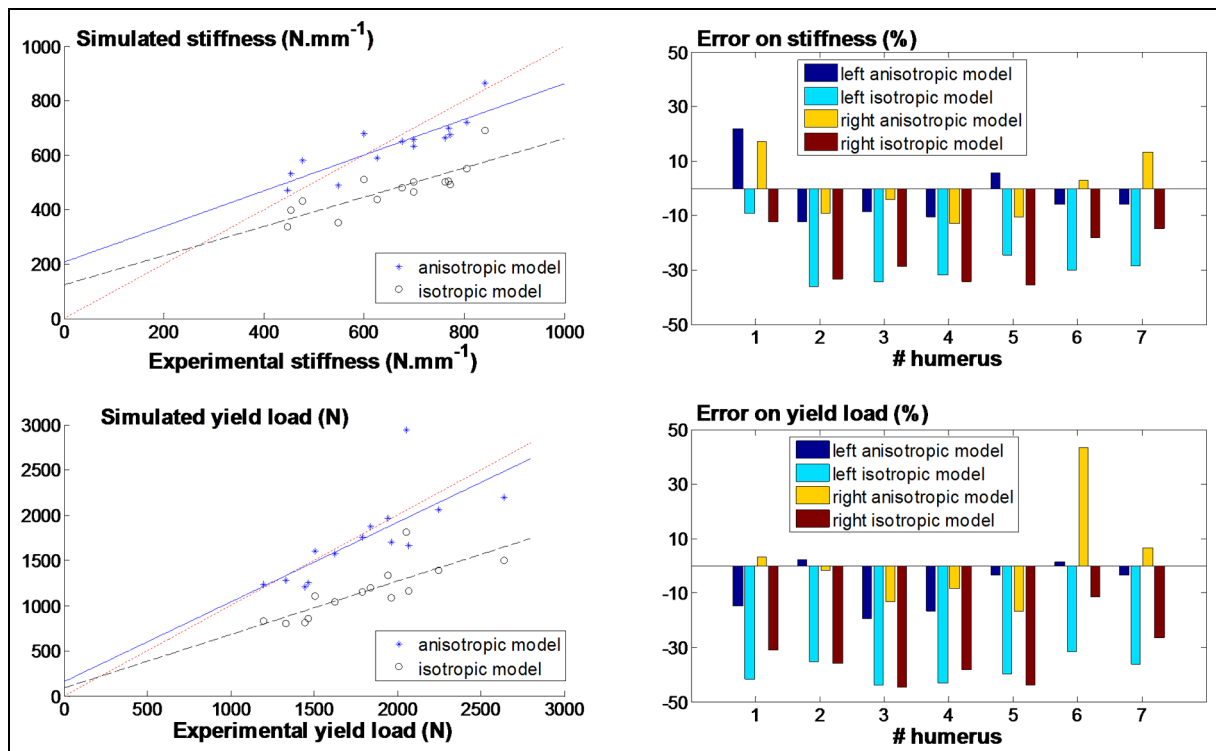


Figure 8. (Left) Experimental versus simulated stiffness and yield load for the 14 bone samples and for both a density-dependent transversely isotropic model and a density-dependent isotropic model. The red dashed line represents a perfect prediction (simulation = experiments). (Right) Prediction error on stiffness and yield load for these two models.

Density–elasticity relationships for canine long bone as a function of dog mass were determined by weighting human relationships from published canine bone properties. Using material parameters from literature only, and not specifically calibrated on the experimental results, the produced models were able to satisfactorily predict bending stiffness and yield load. However, more detailed studies on microstructure or composition of canine bone as a function of mass (or breed) would be required in order to propose a more comprehensive relation.

The predictive power of the models for stiffness values and yield loads is here reflected not only by a good correlation but also by a good concordance, which is less often the case in published models.^{40,41} This therefore suggested that the approach used in this work produces valid models to predict bone stiffness and yield loads in three-point bending of canine long bones.

Comparison between models

The benefit of the non-linear density-dependent transversely isotropic model compared to the two other models is demonstrated in terms of its improved prediction capability. However, it is surprising that the two-material isotropic model leads to better predictions than the density-dependent isotropic model. This may be explained by the fact that during a bending test, the bone is essentially subject to tension and compression, and therefore, the longitudinal modulus of the bone plays a crucial role compared to transverse modulus. In the case of the density-dependent isotropic model, the computed average Young's modulus is therefore underestimated, for a loading involving mainly the longitudinal direction. Predicted stiffness is thus globally underestimated using the density-dependent isotropic model. On the contrary, the two-material model may widely overestimate Young's modulus by considering

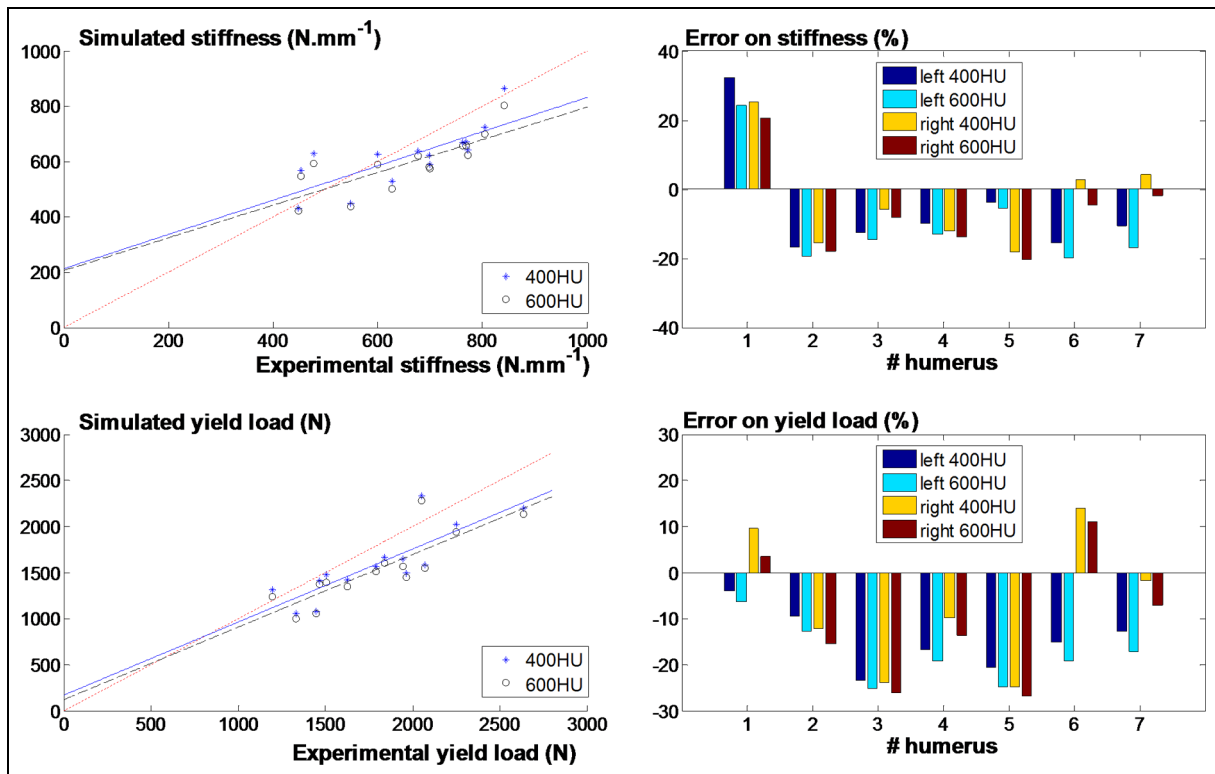


Figure 9. (Left) Experimental versus simulated stiffness and yield load for the 14 bone samples and for a two-material isotropic model. In this model, trabecular and cortical tissues are considered homogeneous and are separated from density thresholds of 400 or 600 HU issued the CT scan. The red dashed line represents a perfect prediction (simulation = experiments). (Right) Prediction error on stiffness and yield load for these two models.

constant density for cortical bone, as it is clearly seen that it is not uniform over the cortical bone (Figure 5). Therefore, it may lead to higher errors in more complex loading modes even without involving a huge overestimation of bone properties in the case of bending loads. For instance, a HU value of 1500 HU for cortical bone corresponds to longitudinal and transverse moduli of 9.7 and 4.7 GPa, respectively, using the density-dependent transversely isotropic model, whereas it corresponds to Young's modulus equal to 7.2 GPa using the density-dependent isotropic model and equal to 15 GPa in the case of the two-material models. One other limitation of the two-material model is the sensitivity of the results to the threshold value chosen to separate trabecular and cortical tissues, which may be user-dependent. This limit obviously disappears when the density-dependent model is used.

As far as the ease of implementation is concerned, computation times were equivalent for the three models. However, density-dependent models require developing an algorithm in order to link HU values to elastic properties and also require a calibration of the CT-scan. Moreover, using a transversely isotropic model requires the definition of orthotropic axis, which has been approximated in our case for bending tests. More complex algorithms would be required to assign local orthotropic axis for more complex loadings. Except for these pre-processing steps, the

calculation of the three types of models is then straightforward.

Limitations and challenges

One of the limitations of bending tests lies in the fact that results depend on the friction coefficient between sample and the bending tools, as illustrated by our sensitivity analysis and by Zeng et al.⁴² Bending stand-resin interaction was modelled with friction coefficient of 0.7 due to the lack of existing values. Even if this friction coefficient is realistic for such a soft resin, experiments could be performed in order to confirm these results. However, such measurements are complex to perform, as long as apparent friction coefficients may be affected by local deformation of the resin due to the cylindrical shape of the bending stand and the high loads involved. These local effects are not taken into account in the simulations, as long as resin blocks have been modelled by a single element. This particular point may be subject to further analyses, for instance, using an inverse approach from similar bending tests on well-known materials.

A simple elastoplastic law with isotropic linear hardening was used as proposed in the literature³³ and associated with a von Mises yield criterion. Even though the use of such a criterion has been questioned,⁴³ no consensus has been clearly found and this criterion

is still widely used.^{34,38,40} The simulated post-yield response did not reproduce the plateau observed experimentally for some samples: it may be therefore concluded that the linear hardening set as 5% of the initial mean modulus as proposed in the literature was excessive and should be age and breed dependent or that a perfectly plastic behaviour might be more representative. Including progressive damage in the model may lead to better results as the physical phenomenon leading to bone non-linear behaviour is most probably related to damage rather than plasticity.^{21,34,38,44}

No distinction was made between cortical and trabecular tissues in the bone material properties characterizing the non-linear behaviour, although the microstructures of these tissues are clearly different. It is likely that here the trabecular tissue do not participate substantially to the bone bending response. The material axes were defined from the mid-line of the diaphysis, as commonly reported in the literature,^{45,46} leading to a global definition of the longitudinal direction. As the segment of interest involved in the bending test was restricted to the bone diaphysis in which the main orthotropic direction does not substantially vary, it is unlikely that this simplification has an effect on the reported results. These two limitations suggest that the validity of the procedure proposed here is thus probably restricted to the bending mode of deformation.

Declaration of conflicting interests

The author(s) declared no potential conflicts of interest with respect to the research, authorship, and/or publication of this article.

Funding

The author(s) disclosed receipt of the following financial support for the research, authorship, and/or publication of this article: The authors would like to acknowledge the Research Council of the University of Lie'ge for having selected this research in their funding programme.

References

1. Kumar K, Mogha IV, Aithal HP, et al. Occurrence and pattern of long bone fractures in growing dogs with normal and osteopenic bones. *J Vet Med A Physiol Pathol Clin Med* 2007; 54: 484–490.
2. Miller CW, Sumner-Smith G, Sheridan C, et al. Using the Unger system to classify 386 long bone fractures in dogs. *J Small Anim Pract* 1998; 39: 390–393.
3. Voss K, Kull MA, Hässig M, et al. Repair of long-bone fractures in cats and small dogs with the Unilock mandible locking plate system. *Vet Comp Orthop Traumatol* 2009; 5: 398–405.
4. Ayyappan S, Shafiuzama M, Ganesh TN, et al. A clinical study on external fixators for long bone fracture management in dogs. *Indian J Vet Surg* 2009; 30: 90–92.
5. Rahal C, Otoni C, Pereira O, et al. Synthesis Pengo System plates for the treatment of long-bone diaphyseal fractures in dogs. *Vet Comp Orthop Traumatol* 2008; 21: 59–63.
6. Dueland R, Johnson K, Roe S, et al. Interlocking nail treatment of diaphyseal long-bone fractures in dogs. *J Am Vet Med Assoc* 1999; 214: 59–66.
7. Palierne S, Asimus E, Mathon D, et al. Geometric analysis of the proximal femur in a diverse sample of dogs. *Res Vet Sci* 2006; 80: 243–252.
8. Dvořák M, Nečas A and Zatloukal J. Complications of long bone fracture healing in dogs: functional and radiological criteria for their assessment. *Acta Vet Brno* 2000; 69: 107–114.
9. Jackson LC and Pacchiana PD. Common complications of fracture repair. *Clin Tech Small Anim Pract* 2004; 19: 168–179.
10. Blake CA, Boudrieau RJ, Torrance BS, et al. Single cycle to failure in bending of three standard and five locking plates and plate constructs. *Vet Comp Orthop Traumatol* 2011; 24: 408–417.
11. Zahn K, Frei R, Wunderle D, et al. Mechanical properties of 18 different AO bone plates and the clamp-rod internal fixation system tested on a gap model construct. *Vet Comp Orthop Traumatol* 2008; 21: 185–194.
12. Nassiri M, MacDonald B and O'Byrne JM. Locking compression plate breakage and fracture non-union: a finite element study of three patient-specific cases. *Eur J Orthop Surg Tr* 2012; 22: 275–281.
13. Oh J-K, Sahu D, Ahn YH, et al. Effect of fracture gap on stability of compression plate fixation: a finite element study. *J Orthop Res* 2010; 28: 462–467.
14. Vajgel A, Camargo IB, Willmersdorf RB, et al. Comparative finite element analysis of the biomechanical stability of 2.0 fixation plates in atrophic mandibular fractures. *J Oral Maxillofac Surg* 2013; 71: 335–342.
15. Bessho M, Ohnishi I, Matsumoto T, et al. Prediction of proximal femur strength using a CT-based nonlinear finite element method: differences in predicted fracture load and site with changing load and boundary conditions. *Bone* 2009; 45: 226–231.
16. Hambli R, Bettamer A and Allaoui S. Finite element prediction of proximal femur fracture pattern based on orthotropic behaviour law coupled to quasi-brittle damage. *Med Eng Phys* 2012; 34: 202–210.
17. Tsouknidas A, Anagnostidis K, Maliaris G, et al. Fracture risk in the femoral hip region: a finite element analysis supported experimental approach. *J Biomech* 2012; 45: 1959–1964.
18. Hambli R and Allaoui S. A robust 3D finite element simulation of human proximal femur progressive fracture under stance load with experimental validation. *Ann Biomed Eng* 2013; 41: 2515–2527.
19. Autefage A, Palierne S, Charron C, et al. Effective mechanical properties of diaphyseal cortical bone in the canine femur. *Vet J* 2012; 194: 202–209.
20. Duprey S, Bruyere K and Verriest J-P. Experimental and simulated flexion tests of humerus. *Int J Crashworthines* 2007; 12: 153–158.
21. Ridha H and Thurner PJ. Finite element prediction with experimental validation of damage distribution in single trabeculae during three-point bending tests. *J Mech Behav Biomed Mater* 2013; 27: 94–106.

22. Varghese B, Short D, Penmetza R, et al. Computed-tomography-based finite-element models of long bones can accurately capture strain response to bending and torsion. *J Biomech* 2011; 44: 1374–1379.
23. Trabelsi N, Yosibash Z, Wutte C, et al. Patient-specific finite element analysis of the human femur: a double-blinded biomechanical validation. *J Biomech* 2011; 44: 1666–1672.
24. Viceconti M, Olsen S, Nolte L-P, et al. Extracting clinically relevant data from finite element simulations. *Clin Biomech* 2005; 20: 451–454.
25. Kalender WA and Suess C. A new calibration phantom for quantitative computed tomography. *Med Phys* 1987; 14: 863–866.
26. Austman RL, Milner JS, Holdsworth DW, et al. The effect of the density-modulus relationship selected to apply material properties in a finite element model of long bone. *J Biomech* 2008; 41: 3171–3176.
27. Fedorov A, Beichel R, Kalpathy-Cramer J, et al. 3D Slicer as an image computing platform for the Quantitative Imaging Network. *Magn Reson Imaging* 2012; 30: 1323–1341.
28. D’Ottrepe V, Boman R and Ponthot J-P. Generating smooth surface meshes from multi-region medical-images. *Int J Numer Method Biomed Eng* 2012; 28: 642–660.
29. Sullivan JF. *Technical physics*. New York: Wiley, 1988.
30. Reilly DT and Burstein AH. The elastic and ultimate properties of compact bone tissue. *J Biomech* 1975; 8: 393–405.
31. Wirtz DC, Schiffers N, Pandorf T, et al. Critical evaluation of known bone material properties to realize anisotropic FE-simulation of the proximal femur. *J Biomech* 2000; 33: 1325–1330.
32. Li S, Demirci E and Silberschmidt VV. Variability and anisotropy of mechanical behavior of cortical bone in tension and compression. *J Mech Behav Biomed Mater* 2013; 21: 109–120.
33. Bayraktar HH, Morgan EF, Niebur GL, et al. Comparison of the elastic and yield properties of human femoral trabecular and cortical bone tissue. *J Biomech* 2004; 37: 27–35.
34. Verhulp E, Van Rietbergen B and Huiskes R. Load distribution in the healthy and osteoporotic human proximal femur during a fall to the side. *Bone* 2008; 42: 30–35.
35. Verim O, Tasgetiren S, Er MS, et al. Anatomical evaluation and stress distribution of intact canine femur. *Int J Med Robot* 2013; 9: 103–108.
36. Boman R and Ponthot J-P. Efficient ALE mesh management for 3D quasi-Eulerian problems. *Int J Numer Meth Eng* 2012; 92: 857–890.
37. Jeunechamps P-P and Ponthot J-P. An efficient 3D implicit approach for the thermomechanical simulation of elastic–viscoplastic materials submitted to high strain rate and damage. *Int J Numer Meth Eng* 2013; 94: 920–960.
38. Mengoni M and Ponthot JP. A generic anisotropic continuum damage model integration scheme adaptable to both ductile damage and biological damage-like situations. *Int J Plasticity* 2015; 66: 46–70.
39. Mengoni M, Voide R, de Bien C, et al. A non-linear homogeneous model for bone-like materials under compressive load. *Int J Numer Method Biomed Eng* 2012; 28: 273–287.
40. Helgason B, Taddei F, Pálsson H, et al. A modified method for assigning material properties to FE models of bones. *Med Eng Phys* 2008; 30: 444–453.
41. Taddei F, Schileo E, Helgason B, et al. The material mapping strategy influences the accuracy of CT-based finite element models of bones: an evaluation against experimental measurements. *Med Eng Phys* 2007; 29: 973–979.
42. Zeng X, Wen S, Li M, et al. Estimating Young’s modulus of materials by a new three-point bending method. *Adv Mater Sci Eng* 2014; 2014: e189423.
43. Doblaré M, García JM and Gómez MJ. Modelling bone tissue fracture and healing: a review. *Eng Fract Mech* 2004; 71: 1809–1840.
44. Burkhart TA, Quenneville CE, Dunning CE, et al. Development and validation of a distal radius finite element model to simulate impact loading indicative of a forward fall. *Proc IMechE, Part H: J Engineering in Medicine* 2014; 228: 258–271.
45. Peng L, Bai J, Zeng X, et al. Comparison of isotropic and orthotropic material property assignments on femoral finite element models under two loading conditions. *Med Eng Phys* 2006; 28: 227–233.
46. Yang H, Ma X and Guo T. Some factors that affect the comparison between isotropic and orthotropic inhomogeneous finite element material models of femur. *Med Eng Phys* 2010; 32: 553–560.